

Distributed Swarm Antenna Arrays for Deep Space Applications^{1, 2}

Marco B. Quadrelli³, Richard Hodges, Victor Vlnrotter,
Saptarshi Bandyopadhyay, Francesco Tassi⁴, Stefano Bevilacqua⁴
Jet Propulsion Laboratory, California Institute of Technology
4800 Oak Grove Dr., Pasadena, CA 91109

Abstract— It is desirable to develop a high Equivalent Isotropically Radiated Power (EIRP), autonomous, distributed, reconfigurable, on-demand Ka/X-band transmit-antenna array using small satellites, for deep-space communication (Mars and beyond). Our work shows that a distributed, free-flying swarm array composed of N CubeSats can not only be phased to provide a coherent beam in Ka/X-band, with performance (mass, power, data rate) comparable to the state-of-the-art Mars Reconnaissance Orbiter (MRO), but with N large, higher performance and data rates can be achieved, assuming a proper intra-swarm metrology system is in place.

TABLE OF CONTENTS

1. INTRODUCTION.....	1
2. SYSTEMS ENGINEERING CONSIDERATIONS.....	2
3. ARRAY GEOMETRIC ERROR ANALYSIS.....	5
4. INTEGRATED MODELING AND SIMULATION.....	8
5. CONCLUSIONS.....	11
APPENDIX	12
ACKNOWLEDGEMENTS.....	12
REFERENCES	12
BIOGRAPHY	13

1. INTRODUCTION

Autonomous spacecraft swarms are emerging as a breakthrough space technology to enable low-cost, highly-reconfigurable apertures with high impact on several areas of science [1] from deep space, such as imaging, remote sensing, solar energy collection, and communication, whose development are often hindered by the high cost of a single large satellite telecommunications system or science instrument. Multifunctional systems, in which multiple subsystems are tightly integrated into one single tile-like

satellite, called TileSats (see Figure 1), can further reduce volume, mass, and cost. Hence, the project aims to develop swarms of small TileSats with multifunctional capabilities to enable new deep space missions. This project is unique even because of tight and systematic integration between swarm guidance and control (G&C) study and impactful applications such as deep space communication and radar science, as enabled by small satellites [14, 15, 16, 17].

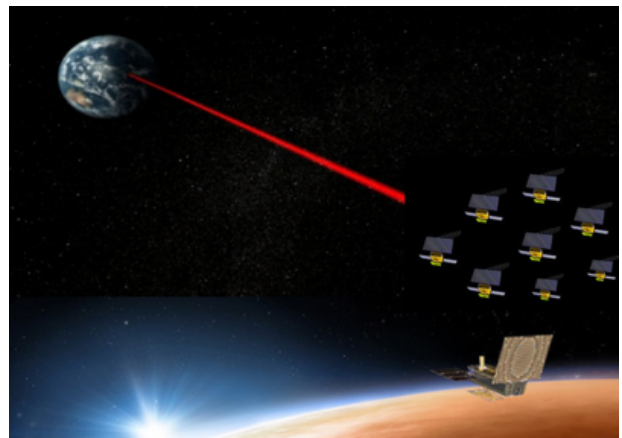


Figure 1 The distributed swarm array.

NASA also has a need for a deep space Ka-band capability to provide high data rate transfer, and at the same time for multifunctional subsystem integration in order to reduce the mass, volume, and power of assets being sent to targets of planetary exploration being executed autonomously [5]. While both Cassini and Juno have a Ka-band capability, the state of the art in deep space Ka-band is MRO and KEPLER. Cassini transmitted and received Ka-band for radio science. Juno has a 2.5 m Ka-band dual reflector antenna, also for radio science. MRO was designed with a full Ka-band capability, and during cruise set a new record (6 Mbps) for the highest Ka-band data rate from a planetary mission. Though it is not used operationally, it has provided much of the validation needed for the deep space system. KEPLER has been using Ka-band routinely for its science downlink for many years. Hence, Ka-band telecom systems have been successfully demonstrated. However, they are limited by power and antenna size – both of which will be

¹ © 2018 California Institute of Technology. Government sponsorship acknowledged. This research was carried out at the Jet Propulsion Laboratory, California Institute of Technology, under a contract with the National Aeronautics and Space Administration.

² Predecisional information for planning and discussion only.

³ Corresponding author, 818-354-7548, marco.b.quadrelli@jpl.nasa.gov

⁴ Visiting Student, Politecnico of Milano, Italy
978-5090-1613-6/17//\$31.00 ©2017 IEEE

addressed by the proposed TileSat architecture. In addition, Cassini used radioisotope power, while MRO, Juno, and KEPLER use very large solar arrays. A cluster (a closely-packed-array) of Ka-band antennas was also proposed for the Jupiter Icy Moons Orbiter in 2004 [8,27] to provide a data rate of 10 Mbps at a maximum distance of 6.5 AU, with 1 mrad pointing accuracy and an effective-isotropic-radiated-power (EIRP) loss of 1.15 dB for a 3-meter diameter antenna. The advantages of multiple apertures compared to a single aperture include: a) electronic beam steering; b) spatial power combining; c) lower power density in the transmit system components; and d) graceful degradation capability. Therefore, it is desirable to develop an autonomous, distributed, reconfigurable swarm transmit array antenna capability that enables a high EIRP, on-demand Ka-band communications system. The benefits to NASA of a swarm system architecture made of N autonomous tiles which can self-organize and reconfigure would include: a) scalable system, upgradable to support future communications demands, b) less vulnerable to single point failure, c) repairable by replacing failed tiles, d) potential for a low cost capability to enable deep space Ka-band communication and science.

In recent years, flight of swarms (100-1000s spacecraft) of FemtoSats (100-gram class spacecraft) has received significant attention, and more recently, formation flying and swarms have been identified as key technologies for development and demonstration. Recent work [23] has focused on the Granular Imager, a game-changing paradigm to design future space imaging systems by means of remote electromagnetic confinement and alignment of a swarm of very small reflectors (FemtoSat-size or less), and appropriate image reconstruction techniques, leading to enormous reduction in cost and system complexity. Used interferometrically, for example [18, 19, 20, 21, 22, 23], imagery or focusing can be synthesized over an enormous scale. This work is also centered on the novel multi-functional TileSat design and its algorithmic and experimental development of autonomous in-space construction of a large connected antenna array for Ka-band deep-space communication. Typically, phased array antennas have a limitation both in pointing accuracy, based on the size and density of the individual elements, and overall cone of pointing.

The goals of this task were to demonstrate that N tiles forming a distributed, free-flying swarm array can be phased to provide a coherent beam in Ka-band, and show that a promising radiofrequency distribution methodology is feasible to enable a phased array with performance (mass, power, data rate) comparable to MRO (Mars Reconnaissance Orbiter). More specifically, the objectives were to: a) Demonstrate feasibility of a scalable autonomous distributed Ka-band antenna swarm array for deep space applications; b) Develop concept of operations for both data link and radar science applications, considering both active and passive radars, based on electromagnetic theory and physical limitations; c) Design the Ka-band antenna array system for effective diameters of up to 10 m, capable of 0.1-1 Gb/s data rates, with direct relevance to interplanetary network goals;

and d) Develop algorithmic techniques for efficient distributed system G&C of the swarm array, including innovative techniques for propellant-less-tether-based autonomous rendezvous and docking for highly efficient proximity operations and self-assembly, and model and simulate them for the multibody modeling and simulation of autonomous system reconfiguration.

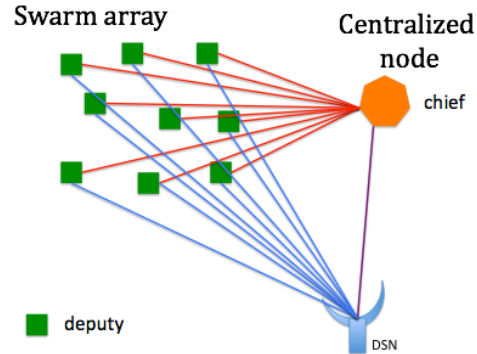


Figure 2 Centralized architecture for the swarm array, including DSN.

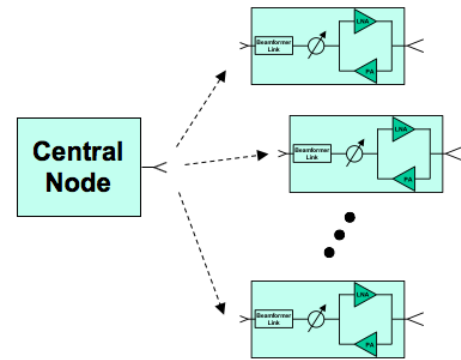


Figure 3 Swarm array configuration with central node.

2. SYSTEMS ENGINEERING CONSIDERATIONS

A large swarm could be assembled in multiple launches as part of forward deployment of equipment and supplies to support a Mars human exploration mission. This concept of operations supports the swarm array scalability, maintenance and repair benefits discussed earlier. Note that the combined transmit/receive architectures could potentially support science activities, assist a UHF ground link to rovers on Mars surface, etc. during periods when high speed telecom capability is not needed.

Monolithic apertures ~3m diameter are in use today on numerous deep space missions. Large aperture deployable mesh reflector antennas >9m diameter are available, but they are significantly more expensive, impose very demanding beam pointing requirements and present stowage challenges. Alternate large aperture technologies (membrane, gossamer, or inflatable type) could stow more compactly, but add additional risks, including lower fault-tolerance, structural vibrations, structural misalignments, tight planarity

requirements, thermo-structural stability, ageing and creep, continuous calibrations, deployment complexities, sub-mm-level surface accuracy in the primary, unavoidable systematic manufacturing errors, material outgassing and surface contamination. The advantages of distributed apertures over single apertures are: the capability of electronic beam steering, spatial power combining, lower power density in the transmit system components, and graceful degradation capability. The disadvantages of distributed apertures over single aperture are: complexity to control and stabilize the structure, high-precision metrology limitations, require precision Attitude Determination and Control System (ACS), accurate clock needed for precise modulation alignment phasing, and possible side lobes due to geometric distortion in element antenna pattern.

A swarm array would replace standard high-power amplifier plus large antenna architecture. In this case, the antenna data rate scales with swarm size. It needs a centralized node to coordinate and manage the overall system (Fig. 2). This system could use a UHF link to distribute time, phase, etc. to array elements, a wireless beamformer and an RF or Laser metrology system. RF, IF, or digital are three beamformer options (Fig. 3). Technical challenges include: a) the need for phased array coherence: the key is to use system such as Phased-Locked Loops (PLL) to synchronize beamformer signals; b) the need to use signal such as a pilot beacon from the DSN (Deep Space Network) to provide synchronization of carrier signal; c) RF or laser metrology for pulse-to-pulse alignment; and d) Timing and signal synchronization.

Multiple reference frames are involved in determining the pointing needs for a swarm away. As a reference, Figure 4 shows the various mechanical reference frames that would be involved in an antenna link budget, and Figure 5 shows the kinematics chain of the reference frames for monolithic and swarm array.

The systems engineering approach in this study included two main tasks: a) Systems Engineering of Antenna Array Concept, and b) Swarm Dynamics and Real-Time Reconfiguration and Steering of Array. Leveraging previous Ka-band system studies from Mars [1], previous space interferometry, formation flying work, and MRO specs, we conducted antenna sensitivity analysis and developed a preliminary Ka-band link budget (Table 1). We also investigated available metrology [3] (Table 2) and array timing/phasing techniques. These data clearly indicate that optical metrology is substantially better than RF.

As a test case to evaluate the performance of a swarm array relative to a large single satellite communications system, we compared MRO to a hypothetical swarm array composed of CubeSats similar to MarCO [27], except operating at Ka-band instead of X-band (see Table 3). Each CubeSat is assumed to have an IRIS radio and 30 x 60 Ka-band reflectarray [2]. A chief/director spacecraft is still needed, and would handle UHF telecom relay and coordination with all “deputy” spacecraft. The link budget in Table 1 shows that the single satellite system and a swarm of ~30 CubeSats are very comparable. The key differences between these two systems are transmit power and antenna

gain, the two parameters that scale with the number of CubeSats in the swarm. To explore this, Figure 6 shows the impact of swarm size on EIRP and relative data rate. As noted earlier, the breakeven point is about 30 CubeSats. More importantly, tripling the number of CubeSats to $N=100$ results in a 10X increase in data rate. Since total power radiated and antenna gain increase in proportion to the number of CubeSats, EIRP (power x gain) increases as the *square* of the number of CubeSats. This comparison clearly shows that high EIRP is feasible with swarm array.

Frames involved

F_J	Inertial Frame
F_{DSN}	DSN frame
F_B	Bus Frame
F_O	Orbit Frame
F_A	Antenna Frame
F_F	Feed Frame
F_S	Star Tracker Frame
F_I	IMU Frame

Figure 4 Frames involved in antenna error budget.

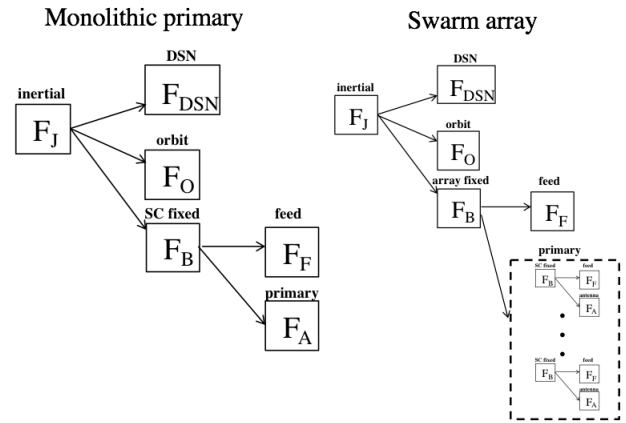


Figure 5 Kinematics chain of frames for monolithic and swarm array.

It is also of interest to evaluate the performance increase that could be achieved by increasing the MRO antenna size. The only practical option to achieve very large (>6m) antenna apertures is a deployable mesh reflector such as the AstroMesh© or Harris folded rib antenna [9, 10, 11]. Table 4 shows a comparison of MRO with current antenna and a 9.5m mesh reflector, which results in a 10X increase in data rate (see Figure 7). However, there is a significant cost increase relative to MRO due to the deployable antenna, increased mass and stowage requirements. Further, this approach may require a larger bus and possibly a fine beam electronic

pointing system to accurately aim the ~ 0.06 degree high gain antenna beam towards a DSN ground station on Earth [9].

Several technology developments are needed to achieve the goal of enabling a practical swarm array antenna system. The most critical items are appropriate timing/sequencing algorithms to cohere array and laser metrology [3] to determine relative s/c positions with sufficient accuracy to carry out the phasing of the array. Phase synchronization, as practiced in the DSN, can be used here and time synchronization is only needed for symbol rate synchronization. This is discussed in more detail in the sections below.

Table 1 Telecomm link budget comparing a swarm array of 30 Ka-band CubeSats to a Monolithic system (MRO).

Link Parameter	Units	Monolithic Aperture	Swarm Array
Transmitter parameters			
Total Transmitter Power	dBm	45.44	48.32
Circuit losses	dB	-0.5	-0.5
S/C Antenna Gain	dB	58.18	55.31
Antenna Pointing Loss	dB	-0.63	-0.63
EIRP	dBm	102.49	102.5
Path parameters			
Space Loss	dB	-294.58	-294.58
Atmospheric Attenuation	dB	-1.18	-1.18
Receiver parameters			
Earth Station Antenna Gain	dB	79.3	79.3
Receiver Circuit Loss Pointing	dB	-0.5	-0.5
Pointing Loss	dB	-0.1	-0.1
Polarization Loss	dB	-0.04	-0.04
Total Power Summary			
Total Received Power	dBm	-114.61	-114.6
Noise Spectral Density	dBm/Hz	-179.18	-179.18
Pt/No	dBm-Hz	64.57	64.58
Data Channel Performance			
Received Pt/No	dB-Hz	64.57	64.58
Pd/No	dB	64.57	64.58
Data Rate	dB	60.79	60.79
Available Eb/No	dB-Hz	3.78	3.79
Radio Loss	dB	-0.1	-0.1
Subcarrier Demod Loss	dB	0	0
Symbol Sync Loss	dB	-0.05	-0.05
Waveform Distortion Loss	dB	-0.15	-0.15
Output Eb/No	dB	3.48	3.49
Required Eb/No	dB	-0.1	-0.1
Performance Margin	dB	3.58	3.59

Table 2 State-of-the-art in metrology techniques for small

spacecraft.

Technology	Accuracy (RMS error)		TRL	Comment	Available to Cubesats
	Range	Bearing			
RF Metrology	4×10^{-3} m (4mm)	3×10^{-4} radians (1 arc minute)	high		Yes
Optical Metrology	1×10^{-6} m (1micrometer)	1×10^{-5} radians (2 arc second)	high	MSTAR	No
LIDARs	Approx. 1mm	Approx. arcminute	low	Vision-based	Yes
RF ranging	1×10^{-6} m (1micrometer)	-	low	ENSCO	Yes

Table 3 System parameters for a comparison of MRO telecom system to hypothetical MarCO-like Ka-band swarm. Data from RF and optical metrology are taken from [3].

	MRO	MarCO CubeSat
Size	S/C Fairing	30x20x10 cm ³
Launch Mass	2180 kg	14 kg
Tx Power	35W	2W
Antenna Size	3m	60 x 30 cm ²
Antenna Gain	56 dB	40 dBic
Antenna type	Parabola	Reflectarray
Deploy antenna?	Yes	Yes

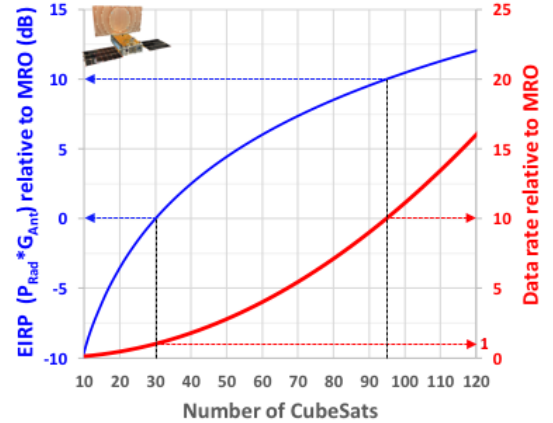


Figure 6 A System parameters for a comparison of MRO telecom system to hypothetical MarCO-like Ka-band swarm. Antenna array EIRP and data rate vs. number of agents, and comparison with MRO.

Table 4 Parameters used to estimate the improvement of MRO telecom system by replacing the 3m composite

reflector with a 9.5m AstroMesh reflector.

	MRO	MRO+AstroMesh
Size	S/C Fairing	Astromesh stow
Antenna Mass	23 kg	55 kg (est*)
Tx Power	35W	35W
Antenna Size	3m	9.5m
Antenna Gain	56 dB	66 dB
Antenna type	Composite	AstroMesh
Questions	MRO bus sufficient for control? S/C pointing system adequate?	

* Assumes 0.75 kg/m² mass density, including boom (TBC)

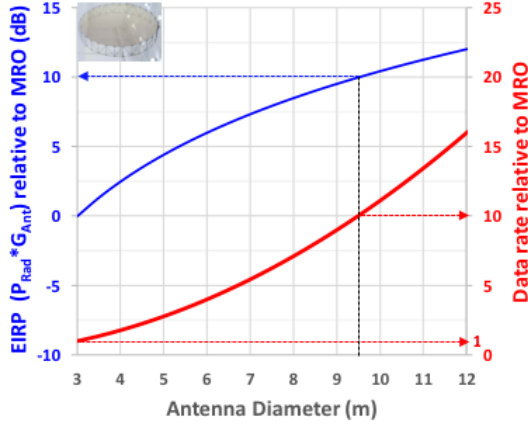


Figure 7 EIRP and data rate vs. monolithic antenna diameter, and comparison with MRO.

3. ARRAY GEOMETRIC ERROR ANALYSIS

The most critical factor in achieving coherence in a Swarm Array is accurate alignment of the phase of the transmitted carrier frequency from each element, or “deputy”, in order to form the desired array beam in the far-field of the deputy’s antennas. It is assumed that the element antennas have been mechanically steered to point in the direction of the intended target, and that only phasing of the carrier remains in order to form an array beam centered on the target. A similar procedure is required when the Swarm Array is used to receive a plane-wave signal from a distant transmitter, except in this case the phases of the received carriers must be aligned to form the array pattern in the desired receive direction. In both cases, the array phase must be first calibrated to phase up the array, then adjusted continuously as the geometry changes due to orbital dynamics. It will be assumed here that orbital dynamics are slow and known well enough to enable predicting and adjusting the differential phase between elements to the required accuracy, as the geometry changes. In this section a geometric model of the Swarm Array will be developed, error sources identified, and their impact on Swarm Array performance determined. Focus will be on the transmit mode of operation, however the analysis applies equally to receive mode as well.

The Swarm Array geometry is shown in Figure 8, in Cartesian coordinates centered on the “chief” element, which is taken to be the reference element in the array, with sufficient storage, computing power and metrology capability to enable maintaining and adjusting the state of the array as conditions change. It will be assumed that the array elements, or deputies, are all phased up with respect to the carrier phase of the chief, such that the carriers from each element are in phase in the far-field of the array. The chief element is located at the center of the Cartesian coordinate system, defined by the orthogonal unit vectors $(\hat{i}, \hat{j}, \hat{k})$,

where the \hat{k} component is parallel to the “line-of-sight” (or LOS) vector to the target. In an array of N elements, including the chief, there are $N-1$ deputies, designated in Figure 8 as deputy #1, deputy #2, and so on, each located at a bearing and distance defined by the corresponding position vectors $\vec{p}_1, \vec{p}_2, \dots, \vec{p}_{N-1}$. However, in our model the stored locations of the deputies in the chief’s computer may be slightly different, given by the position vectors $\vec{p}_1, \vec{p}_2, \dots, \vec{p}_{N-1}$, hence there is an error between the stored positions and the true positions, given by the error vector $\vec{r}_1, \vec{r}_2, \dots, \vec{r}_{N-1}$. These errors will cause the deputy’s phases to be misadjusted, reducing the array gain over that achievable with ideal phasing. We proceed to determine the magnitude of these errors based on a simple model for the error distribution, using actual values for the error variance in practical state-of-the-art range and bearing metrologies. Finally, the error variances will be used to evaluate array loss due to position errors, using several different candidate metrologies as examples.

The position vectors of the deputies in Cartesian coordinates are $\vec{p}_1 = p_{1,x}\hat{i} + p_{1,y}\hat{j} + p_{1,z}\hat{k}$, $\vec{p}_2 = p_{2,x}\hat{i} + p_{2,y}\hat{j} + p_{2,z}\hat{k}$, ..., whereas the error vectors can be expressed as $\vec{r}_1 = r_{1,x}\hat{i} + r_{1,y}\hat{j} + r_{1,z}\hat{k}$, $\vec{r}_2 = r_{2,x}\hat{i} + r_{2,y}\hat{j} + r_{2,z}\hat{k}$, True position vectors are the vector sum of the stored position and error vectors, yielding $\vec{P}_1 = \vec{p}_1 + \vec{r}_1$, $\vec{P}_2 = \vec{p}_2 + \vec{r}_2$, For a compact Swarm Array operating over interplanetary distances, only the projection of the position vectors onto the LOS vector contribute to array phase, since the array diameter is much smaller (by about 20 orders of magnitude) than the distance to the target. Referring to Figure 8, this can be seen by writing out the Euclidian distance from the first deputy to the target in terms of the stored vector and error vector components as in equation (1),

$$\begin{aligned}
|\vec{R}_1| &= |\vec{R} - \vec{P}_1| = | [R - (p_{1,z} + r_{1,z})] \hat{k} - (p_{1,x} + r_{1,x}) \hat{i} - (p_{1,y} + r_{1,y}) \hat{j} | \\
&= \sqrt{[R - (p_{1,z} + r_{1,z})]^2 + (p_{1,x} + r_{1,x})^2 + (p_{1,y} + r_{1,y})^2} \\
&= [R - (p_{1,z} + r_{1,z})] \sqrt{1 + \frac{(p_{1,x} + r_{1,x})^2}{[R - (p_{1,z} + r_{1,z})]^2} + \frac{(p_{1,y} + r_{1,y})^2}{[R - (p_{1,z} + r_{1,z})]^2}} \\
&\cong [R - (p_{1,z} + r_{1,z})] = R - \vec{P}_1 \cdot \hat{k} \\
(1)
\end{aligned}$$

and recognizing that due to the enormous distances between planets (~ 1 AU) the second and third terms inside the normalized square-root are $O(10^{-10})$ and hence can be ignored. Generalizing to the n -th element, the range difference to the target between the n -th deputy and the chief, ΔR_n , is the projection of the n -th position vector \vec{P}_n onto the LOS unit vector \hat{k} : $\Delta R_n = R - R_n = \vec{P}_n \cdot \hat{k} = p_{n,z} + r_{n,z}$. Similarly, the phase error of the n -th array element relative to the phase of the chief is a scaled version of the projected range error, $r_{n,z}$, which is in turn the projection of the error vector onto the LOS unit vector \hat{k} : $r_{n,z} = \Delta R_n - p_{n,z} = (\vec{P}_n - \vec{p}_n) \cdot \hat{k}$.

In the language of spacecraft metrology, errors are typically specified in terms of “range” and azimuth/elevation (AZ,EL) “bearing” components, implying the use of spherical instead of Cartesian coordinates. Therefore, in order to compute the projection of the error vector onto the

LOS, assumed to be in the \hat{k} direction, it is necessary to first convert from spherical to Cartesian coordinates.

The relationship between Cartesian and spherical coordinates is illustrated in Figure 9, where the true position vector \vec{P} is shown in the reduced two-dimensional (\hat{j}, \hat{k}) plane for simplicity. In general, the true position vector can be described in Cartesian coordinates as $\vec{P} = P_x \hat{i} + P_y \hat{j} + P_z \hat{k}$. In spherical coordinates, the true position vector \vec{P} is described in terms of the three locally orthogonal spherical coordinates $(\hat{\rho}, \hat{\theta}, \hat{\phi})$ as $\vec{P}_s = P_\rho \hat{\rho} + P_\theta \hat{\theta} + P_\phi \hat{\phi}$. Adding the error vector \vec{r} to the true position vector \vec{P} yields the stored position vector $\vec{p} = \vec{P} + \vec{r} = (P_x + r_x) \hat{i} + (P_y + r_y) \hat{j} + (P_z + r_z) \hat{k} = p_x \hat{i} + p_y \hat{j} + p_z \hat{k}$. The stored position vector can be expressed in spherical coordinates as $\vec{p}_s = p_\rho \hat{\rho} + p_\theta \hat{\theta} + p_\phi \hat{\phi}$.

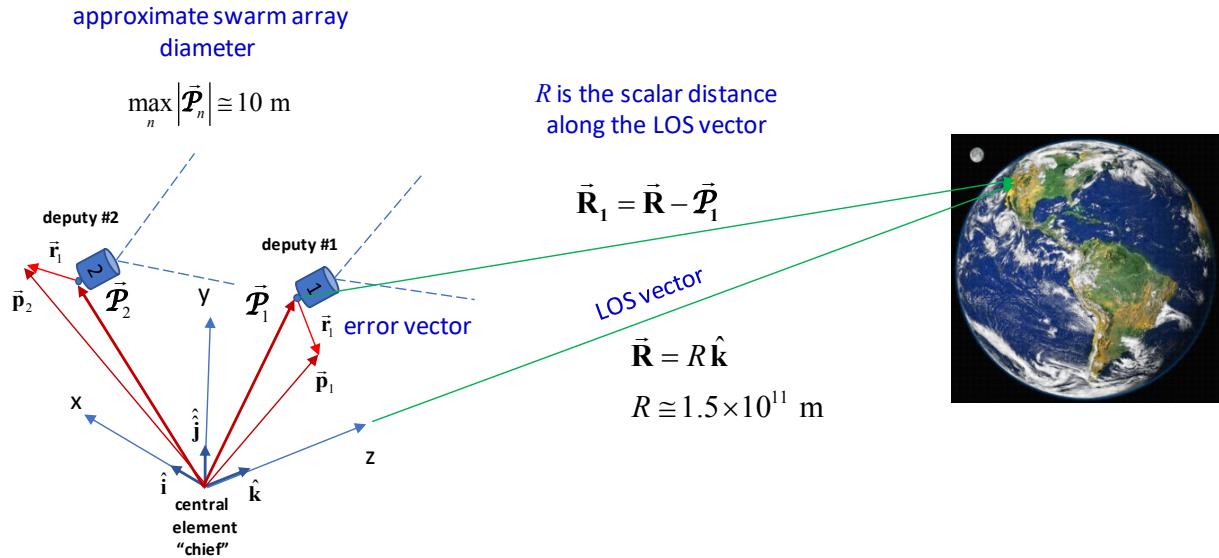


Figure 8 Swarm array geometry and definition of key vector components, in Cartesian coordinates. In this hypothetical scenario the Swarm Array is in orbit around Mars, transmitting to Earth at a distance of roughly 1 AU.

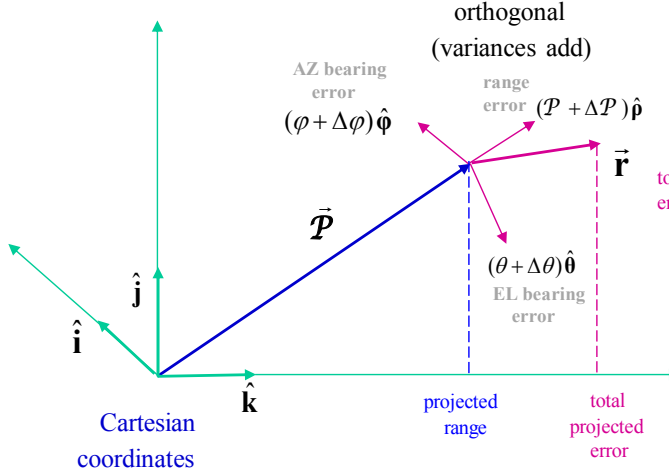


Figure 9 Position and error vectors in spherical coordinates.

In general, the conversion between Cartesian and spherical coordinates can be described via the following matrix transformation, which specifies the Cartesian coefficients $\mathbf{a} = (a_x, a_y, a_z)$ in terms of spherical coordinates $\mathbf{a}_s = (a_\rho, a_\theta, a_\phi)$, and vice versa, as $\mathbf{a}^T = \mathbf{A}\mathbf{a}_s^T$ and $\mathbf{a}_s^T = \mathbf{A}_s\mathbf{a}^T$ respectively. The transformation matrices \mathbf{A} and \mathbf{A}_s are

$$\mathbf{A} = \begin{bmatrix} \sin \theta \cos \phi & \cos \theta \cos \phi & -\sin \phi \\ \sin \theta \sin \phi & \cos \theta \sin \phi & \cos \phi \\ \cos \theta & -\sin \theta & 0 \end{bmatrix}$$

$$\mathbf{A}_s = \begin{bmatrix} \sin \theta \cos \phi & \sin \theta \sin \phi & \cos \phi \\ -\cos \theta \cos \phi & \cos \theta \sin \phi & -\sin \phi \\ -\sin \theta & \cos \theta & 0 \end{bmatrix}$$

The position vectors in the chief spacecraft's computer are stored in Cartesian coordinates, which can also be expressed in terms of spherical coordinates referred to the underlying Cartesian coordinate system. For example, the true position vector can be expressed in spherical coordinates as

$$\bar{\mathbf{P}} = P_\rho \hat{\mathbf{p}} + P_\theta \hat{\mathbf{\theta}} + P_\phi \hat{\mathbf{\phi}}$$

$$P_\rho = \sqrt{P_x^2 + P_y^2 + P_z^2}, \quad P_\theta = \arccos(P_z/P_\rho), \quad P_\phi = \arctan(P_y/P_x)$$

where (P_x, P_y, P_z) are the original Cartesian coefficients.

Referring to Figure 9, we can see that the spherical coordinates of the stored position vector can be expressed in spherical coordinates as

$$\begin{bmatrix} P_\rho \\ P_\theta \\ P_\phi \end{bmatrix} = \begin{bmatrix} \sin(\theta + \Delta\theta) \cos(\phi + \Delta\phi) & \sin(\theta + \Delta\theta) \sin(\phi + \Delta\phi) & \cos(\phi + \Delta\phi) \\ -\cos(\theta + \Delta\theta) \cos(\phi + \Delta\phi) & \cos(\theta + \Delta\theta) \sin(\phi + \Delta\phi) & -\sin(\phi + \Delta\phi) \\ -\sin(\theta + \Delta\theta) & \cos(\theta + \Delta\theta) & 0 \end{bmatrix} \begin{bmatrix} P_x \\ P_y \\ P_z \end{bmatrix}$$

Assuming the errors in range and bearing are small enough to validate the approximations $\theta + \Delta\theta \cong \theta$ and $\phi + \Delta\phi \cong \phi$ in the matrix transformations, it follows that

$$\begin{bmatrix} P_\rho & P_\theta & P_\phi \end{bmatrix} = \mathbf{A}_s \begin{bmatrix} P_x & P_y & P_z \end{bmatrix},$$

$$\begin{bmatrix} P_\rho & P_\theta & P_\phi \end{bmatrix}^T \cong \mathbf{A}_s \left\{ \begin{bmatrix} P_x & P_y & P_z \end{bmatrix}^T + \begin{bmatrix} r_x & r_y & r_z \end{bmatrix}^T \right\}$$

and therefore $\mathbf{r}_s \cong \mathbf{A}_s(\mathbf{p} - \mathbf{P}) = \mathbf{A}_s \mathbf{r} = \begin{bmatrix} r_\rho & r_\theta & r_\phi \end{bmatrix}^T$.

Within the bounds of the above approximations, the error vector in spherical coordinates is simply the matrix transformation of the error coordinates in Cartesian coordinates. Likewise, if the spherical coordinates are specified, the inverse transformation yields the Cartesian error coordinates $\mathbf{r} = \begin{bmatrix} r_x & r_y & r_z \end{bmatrix}^T$.

Metrology errors are typically expressed in terms of range and bearing errors as shown in Fig. 2, where current state-of-the-art RMS errors are specified for both RF and optical metrologies. The spherical error components are inherently random variables. We are ultimately interested in finding the projection of the total RMS error onto the LOS direction vector $\hat{\mathbf{k}}$, which was shown to be the relevant error source affecting Swarm Array losses when operating over interplanetary distances. This can be accomplished by first conditioning on the error components, determining the projection of the given error-corrupted position vector onto the $\hat{\mathbf{k}}$ direction, and averaging the resulting projected vector to determine the relevant component of total RMS error. The projection of the total error vector expressed in spherical coordinates, $\bar{\mathbf{r}}_s$, onto the LOS direction vector can be determined via the inverse transformation as $\bar{\mathbf{r}}_s \cdot \hat{\mathbf{k}} = \Delta P_\rho \cos(\theta) - \Delta P_\theta \sin(\theta)$. Note that only the range and elevation vectors project onto the $\hat{\mathbf{k}}$ direction, whereas the azimuth angle does not. This is because the azimuth component rotates the position vector around the LOS direction to form a cone whose tip is at the origin, hence its projection onto the $\hat{\mathbf{k}}$ vector is independent of the azimuth angle. This implies that any bearing error in the azimuth direction will not contribute to the projection, hence can be ignored since it does not impact Swarm Array performance. Only the range errors and elevation errors contribute to the projected error.

The relevant range and bearing errors, ΔP_ρ and ΔP_θ respectively, are independent random variables, having been generated by different instruments. Since the range and bearing errors are independent their

variances add, hence the total variance is the sum of the individual variances, scaled by the elevation-dependent coefficients. Therefore, the total elevation-dependent variance can be expressed as $\sigma_t^2(\theta) = \sigma_\rho^2(\theta) + \sigma_\theta^2(\theta)$,

where $\sigma_\rho^2(\theta) = \cos^2(\theta)E(\Delta\mathcal{P}_\rho^2)$ and $\sigma_\theta^2(\theta) = \sin^2(\theta)E(\Delta\mathcal{P}_\theta^2)$. The RMS errors are measured in meters, which need to be converted to radians of carrier phase in order to determine array loss. For a carrier wavelength of λ meters, a total projected RMS error of $\sigma_t(\theta)$ meters yields an RMS error of $\frac{2\pi}{\lambda}\sigma_t(\theta)$ in radians, or a total error variance of $\sigma^2(\theta) = (\frac{2\pi}{\lambda})^2\sigma_t^2(\theta)$ in radians².

Using the results for array loss in terms of the phase error variance derived in [4], and assuming that the phase error variance is statistically identical for each of $(N-1)$ deputies, the arrayed power P_N can be expressed as $P_N = P_0\{N + N(N-1)\exp[-\sigma^2(\theta)]\}$, where P_0 is the received power from a single deputy. The ideal power for a perfectly phased array of N antennas corresponding to the case $\sigma^2(\theta) = 0$ is clearly P_0N^2 , hence the array loss due to imperfect phasing can be expressed as

$$\Gamma = \frac{N + N(N-1)\exp[-\sigma^2(\theta)]}{N^2}. \text{ Note that in the limit}$$

as $N \rightarrow \infty$ the array loss approaches $\Gamma_\infty = \exp[-\sigma^2(\theta)]$

As an example, consider the RF measurement errors in Fig. 8 for an X-band wavelength of 4 cm, or 0.04 m, at an elevation of 45 degrees where $\sin(45^\circ) = \cos(45^\circ) = \sqrt{2}$. Using the values of the range and bearing variances from Fig. 2 of $E(\Delta\mathcal{P}_\rho^2) = 16 \times 10^{-6} \text{ m}^2$ and $E(\Delta\mathcal{P}_\theta^2) = 9 \times 10^{-8} \text{ m}^2$,

it follows that $\sigma_t^2(45^\circ) = \frac{1}{2}(16 \times 10^{-6} + 0.09 \times 10^{-6}) = 8.045 \times 10^{-6} \text{ m}^2$.

Scaling for squared radians in fractional wavelengths yields $\sigma^2(45^\circ) = (\frac{2\pi}{\lambda})^2\sigma_t^2(45^\circ) = (2.4674 \times 10^4)(8.045 \times 10^{-6}) = 0.1985 \text{ rad}^2$.

Substituting into the expression for array loss for an array of $N = 7$ elements yields an array loss of $\Gamma = \frac{N + N(N-1)\exp[-\sigma^2(\theta)]}{N^2} = \frac{7 + 42\exp[-0.1985]}{79} = 0.8457$

or $\Gamma_{dB} = -0.7278 \text{ dB}$. For this example, the asymptotic limit as $N \rightarrow \infty$ becomes $\Gamma_\infty = \exp[-0.1985] = 0.82$ or $\Gamma_{\infty, dB} = -0.8619 \text{ dB}$. Array power and array loss for RF metrology is shown in Figure 10, and in Figure 11 for Optical metrology, assuming an elevation angle of 90° .

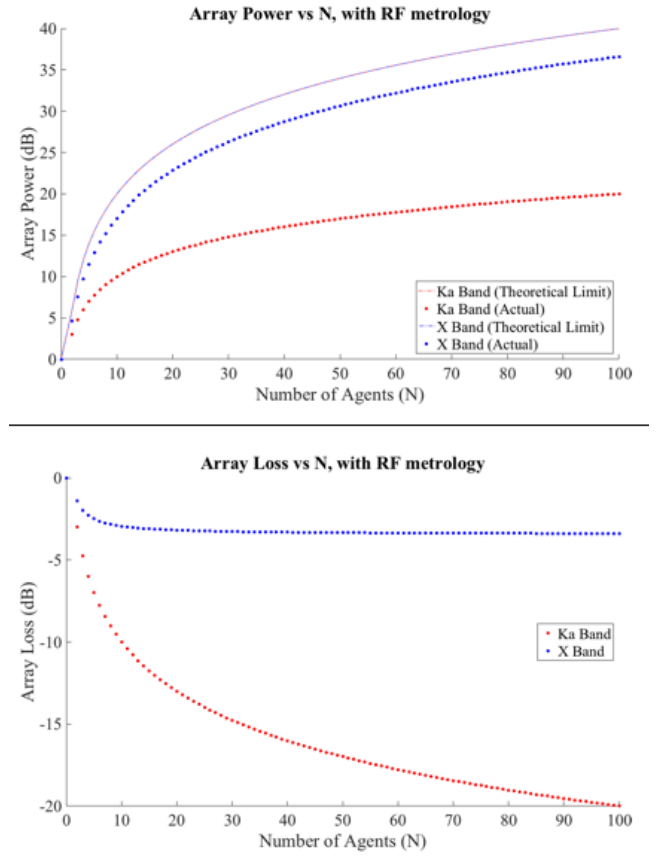


Figure 10 Array power and array loss as a function of number of elements for RF metrology.

4. INTEGRATED MODELING AND SIMULATION

In support of the systems engineering analysis describe above, we have developed and tested a modeling and simulation environment for an antenna array in Mars orbit which integrates the orbital dynamics of the swarm and models the array electromagnetics. Previous related work is in [12, 13]. Figure 12 shows the orbital geometry of the swarm problem. Figure 13 shows a snapshot of the three-dimensional motion of the swarm in Mars' orbit. The equations of motion of the swarm are derived in [24], but are summarized here next. They include the equations of motion of the Chief spacecraft, including oblateness (J_2) and aerodynamic drag, as follows (r =position, v =velocity, h =orbit momentum, Ω =longitude of ascending node, i =inclination, θ =true anomaly, C =aerodynamic constant, k_{J_2} =oblateness coefficient):

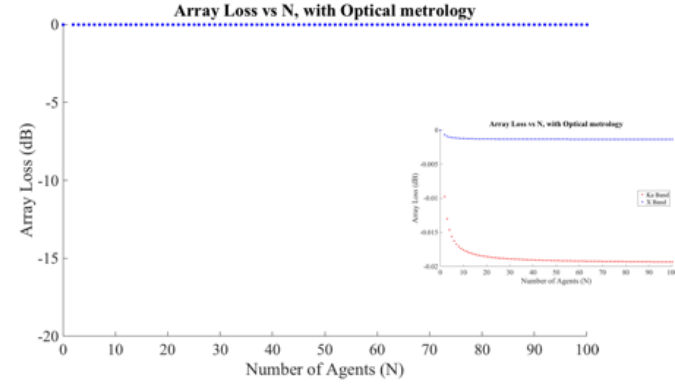
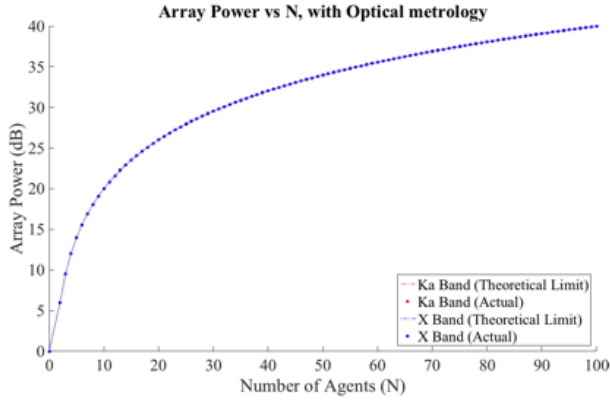


Figure 11 Array power and array loss as a function of number of elements for Optical metrology.

$$\begin{aligned}
 \dot{r} &= v_x, \\
 \dot{v}_x &= -\frac{\mu}{r^2} + \frac{h^2}{r^3} - \frac{k_{J2}}{r^4} (1 - 3 \sin^2 i \sin^2 \theta) - C \|V_a\| v_x, \\
 \dot{h} &= -\frac{k_{J2} \sin^2 i \sin 2\theta}{r^3} - C \|V_a\| (h - \omega_e r^2 \cos i), \\
 \dot{\Omega} &= -\frac{2k_{J2} \cos i \sin^2 \theta}{hr^3} - \frac{C \|V_a\| \omega_e r^2 \sin 2\theta}{2h}, \\
 \dot{i} &= -\frac{k_{J2} \sin 2i \sin 2\theta}{2hr^3} - \frac{C \|V_a\| \omega_e r^2 \sin i \cos^2 \theta}{h}, \\
 \dot{\theta} &= \frac{h}{r^2} + \frac{2k_{J2} \cos^2 i \sin^2 \theta}{hr^3} + \frac{C \|V_a\| \omega_e r^2 \cos i \sin 2\theta}{2h}.
 \end{aligned}$$

and the equations of motion of the N deputy spacecraft as follows [25] (x, y, z =deputy position components in orbiting frame relative to chief, ω_x, ω_z =orbital frequencies):

$$\begin{aligned}
 \ddot{x}_j &= 2\dot{y}_j \omega_z - x_j(\eta_j^2 - \omega_z^2) + y_j \alpha_z - z_j \omega_x \omega_z \\
 &\quad - (\zeta_j - \zeta) \sin i \sin \theta - r(\eta_j^2 - \eta^2) \\
 &\quad - C_j \|V_{aj}\| (\dot{x}_j - y_j \omega_z) \\
 &\quad - (C_j \|V_{aj}\| - C \|V_a\|) v_x \\
 \ddot{y}_j &= -2\dot{x}_j \omega_z + 2\dot{z}_j \omega_x - x_j \alpha_z - y_j(\eta_j^2 - \omega_z^2 - \omega_x^2) + z_j \alpha_x \\
 &\quad - (\zeta_j - \zeta) \sin i \cos \theta \\
 &\quad - C_j \|V_{aj}\| (\dot{y}_j + x_j \omega_z - z_j \omega_x) \\
 &\quad - (C_j \|V_{aj}\| - C \|V_a\|) \left(\frac{h}{r} - \omega_e r \cos i \right)
 \end{aligned}$$

$$\begin{aligned}
 \ddot{z}_j &= -2\dot{y}_j \omega_x - x_j \omega_x \omega_z - y_j \alpha_x - z_j(\eta_j^2 - \omega_x^2) \\
 &\quad - (\zeta_j - \zeta) \cos i - C_j \|V_{aj}\| (\dot{z}_j + y_j \omega_x) \\
 &\quad - (C_j \|V_{aj}\| - C \|V_a\|) \omega_e r \cos \theta \sin i
 \end{aligned}$$

where the following terms are defined as:

$$\begin{aligned}
 \zeta &= \frac{2k_{J2} \sin i \sin \theta}{r^4}, \\
 \zeta_j &= \frac{2k_{J2} r_{jz}}{r_j^5}, \\
 \eta^2 &= \frac{\mu}{r^3} + \frac{k_{J2}}{r^5} - \frac{5k_{J2} \sin^2 i \sin^2 \theta}{r^5}, \\
 \eta_j^2 &= \frac{\mu}{r_j^3} + \frac{k_{J2}}{r_j^5} - \frac{5k_{J2} r_{jz}^2}{r_j^7}, \\
 r_j &= \sqrt{(r + x_j)^2 + y_j^2 + z_j^2}, \\
 r_{jz} &= (r + x_j) \sin i \sin \theta + y_j \sin i \cos \theta + z_j \cos i, \\
 \alpha_z &= -\frac{2h v_x}{r^3} - \frac{k_{J2} \sin^2 i \sin 2\theta}{r^5}, \\
 \alpha_x &= -\frac{k_{J2} \sin 2i \cos \theta}{r^5} + \frac{3v_x k_{J2} \sin 2i \sin \theta}{hr^4} \\
 &\quad - \frac{8k_{J2}^2 \sin^3 i \cos i \sin^2 \theta \cos \theta}{h^2 r^6}.
 \end{aligned}$$

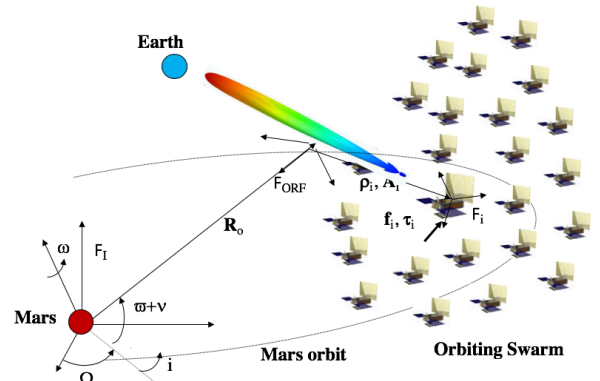


Figure 12 Orbital geometry of swarm problem.

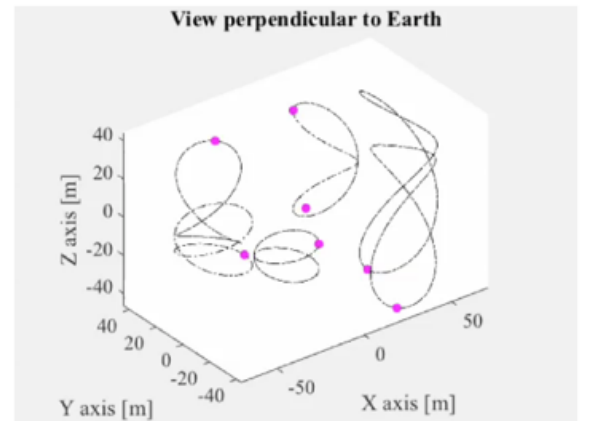


Figure 13 Three-dimensional motion of swarm in Mars'

orbit.

The array is modeled as a collection of N rectangular patches [25], where the electric field of each patch has the following components ($k=2\pi/\lambda$, λ =wavelength)

$$E_\theta = \sin(\phi) \cdot \frac{\sin X}{X} \cdot \frac{\sin Y}{Y} \quad X = \frac{ka}{2} \cdot \sin(\theta) \cdot \sin(\phi)$$

$$E_\phi = \cos(\theta) \cdot \cos(\phi) \cdot \frac{\sin X}{X} \cdot \frac{\sin Y}{Y} \quad Y = \frac{kb}{2} \cdot \sin(\theta) \cdot \cos(\phi)$$

If is $F_n(\theta_n, \phi_n)$ the element pattern function, (A_n, β_n) are the amplitude and phase, the total field emitted by the array at a generic point in polar coordinates (r_n, θ_n, ϕ_n) is

$$E_{tot}(\theta, \phi) = \sum_{n=1}^N A_n F_n(\theta_n, \phi_n) e^{-j(k \cos \theta_n + \beta_n)}$$

Figure 14 shows the three-dimensional swarm with pencil beam from electromagnetic signal, and Figure 15 shows a polar plot of electric field emitted by array.

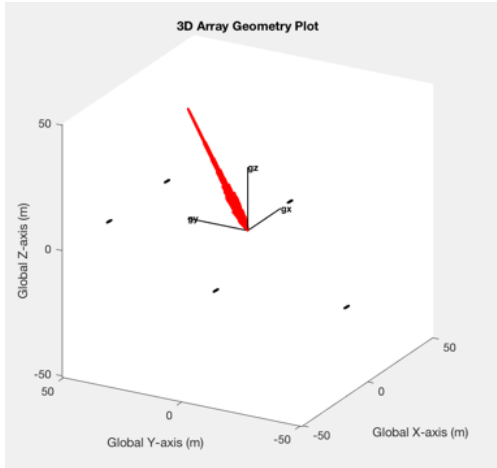


Figure 14 Three-dimensional swarm with pencil beam from electromagnetic signal.

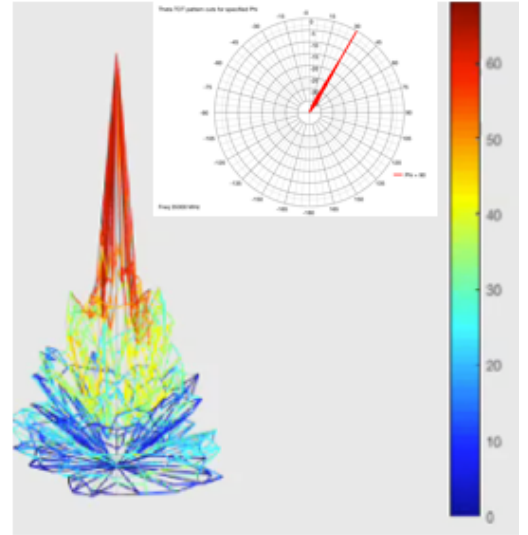


Figure 15 Polar plot of electric field emitted by array.

We have also developed swarm reconfiguration algorithms with functionalities including collision-avoidance, and a simulator for tethered proximity operations, assuming the swarm elements are mechanically connected. A distributed guidance and control algorithm for the reconfiguration of the robotic swarm is introduced in [6, 26], that allows to solve for the collision-free trajectory generation. Figure 16 shows the reconfiguration of $N=10$ spacecraft from a stack into a paraboloidal shape. Figure 17 shows collision-free trajectories for $N=10$ elements, considering an objective function that minimizes the control efforts. Finally, Figure 18 shows the relative angle between tethers for open and closed configurations of the swarm away, assuming the elements of the array are connected by tethers [7], indicating a more precise system response in the closed configuration.

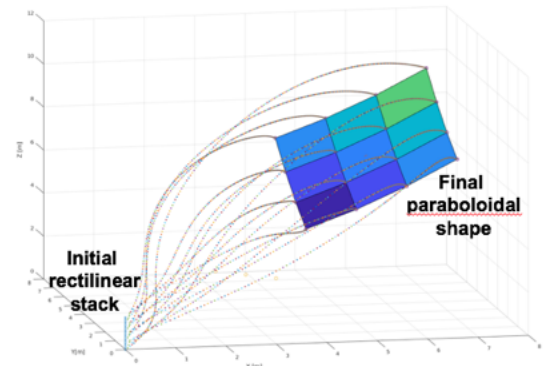


Figure 16 Reconfiguration of $N=10$ spacecraft from a stack into a paraboloidal shape.

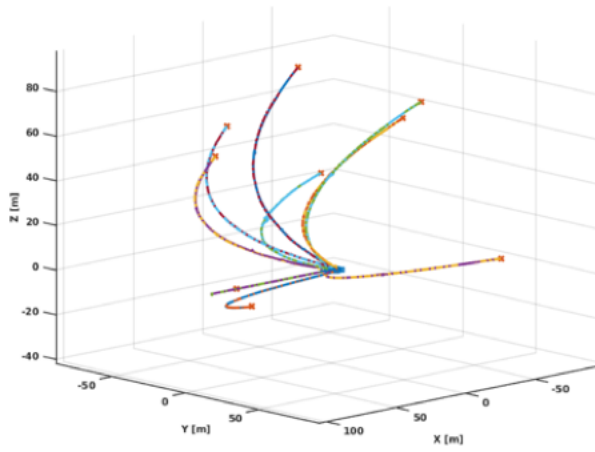


Figure 17 N=10 elements collision-free trajectories, considering an objective function that minimizes the control efforts.

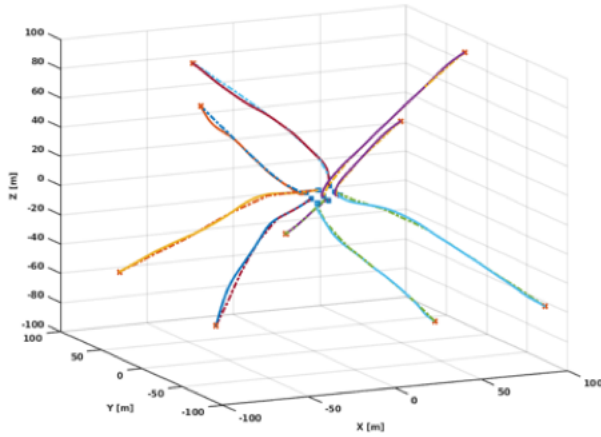
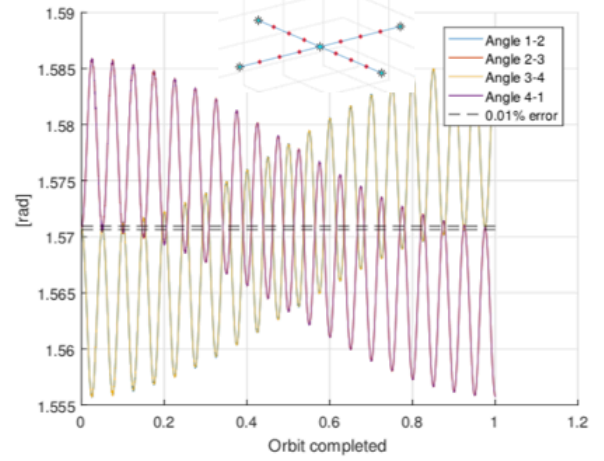
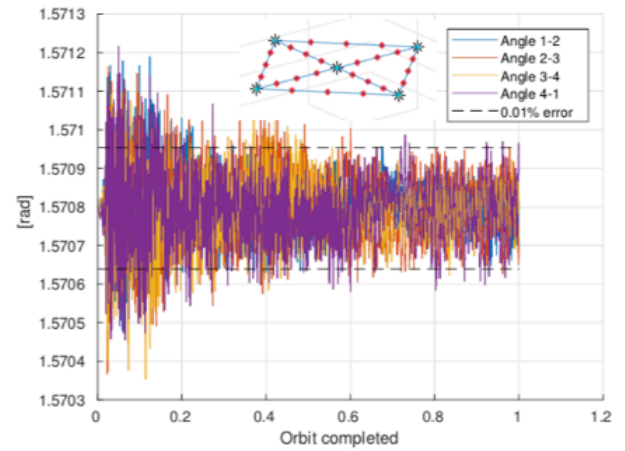


Figure 18 N=10 elements collision-free trajectories, considering an objective function that minimizes the control efforts and the overall distance.



(a) Open configuration



(b) Closed configuration

Figure 19 Relative angle between tethers for open and closed configuration.

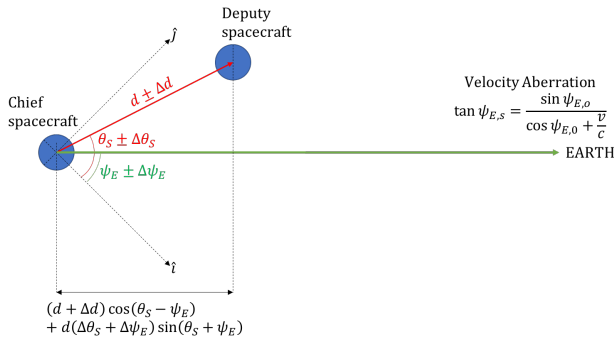
5. CONCLUSIONS

NASA has a need for deep space high data rate transfer, and at the same time for multifunctional subsystem integration in order to reduce the mass, volume, and power of autonomous assets being sent to targets of planetary exploration. This capability will improve entire classes of future JPL missions, with benefits to key challenges in multiple directorates. Combining transmit and receive architectures would also benefit science. A large swarm could be assembled in multiple launches, possibly as part of launches sent in preparation for a future human exploration of Mars. On-going miniaturization in power electronics would make a compelling business case. The main conclusion of this study is that a high data rate downlink swarm array at Mars is feasible. Approximately 30 MarCO CubeSats can achieve MRO-level performance, and ~100 MarCO CubeSats achieve 10X MRO-level performance. Spacecraft could be incrementally added to the swarm, with each launch. Therefore, no dedicated launch would be necessary. Future work includes the further development of metrology options: current RF and Optical metrology options are for big spacecraft (100-kg class)[4]; and we need to further develop

metrology options for small spacecraft. Also, time synchronization options need to be developed, as they closely relate to the metrology.

APPENDIX

Here we present an alternate derivation of the swarm array geometric error analysis. Let d represent the distance from the chief to the deputy, and Δd represent its error. Let θ_S represent the bearing angle from the chief to the deputy, and $\Delta\theta_S$ represent its error. Let ψ_E represent the bearing angle from the chief to the Earth, and $\Delta\psi_E$ represent its error. The reference frame and variables are shown in the figure below.



The time delay distance between the signal from chief and deputy to reach Earth is given by the dot product between $(d + \Delta d)(\cos(\theta_S \pm \Delta\theta_S)\hat{i} + \sin(\theta_S \pm \Delta\theta_S)\hat{j})$ and $(\cos(\psi_E \pm \Delta\psi_E)\hat{i} + \sin(\psi_E \pm \Delta\psi_E)\hat{j})$, which is given by:

Time Delay Distance

$$= (d + \Delta d)\cos(\theta_S - \psi_E) + d(\Delta\theta_S + \Delta\psi_E)\sin(\theta_S + \psi_E),$$

using small angle approximations and neglecting higher-order terms. Therefore, the desired phase difference and timing difference are given by:

Desired Phase Difference

$$= \frac{(d + \Delta d)\cos(\theta_S - \psi_E) + d(\Delta\theta_S + \Delta\psi_E)\sin(\theta_S + \psi_E)}{\lambda},$$

Desired Timing Difference

$$= \frac{(d + \Delta d)\cos(\theta_S - \psi_E) + d(\Delta\theta_S + \Delta\psi_E)\sin(\theta_S + \psi_E)}{c},$$

where λ is the wavelength and c is the speed of light.

Assuming that the errors are Gaussian random variables, given by:

$$\begin{aligned} \Delta d &\sim \mathcal{N}(\mu_{\Delta d}, \sigma_{\Delta d}^2), \\ \Delta\theta_S &\sim \mathcal{N}(\mu_{\Delta\theta_S}, \sigma_{\Delta\theta_S}^2), \\ \Delta\psi_E &\sim \mathcal{N}(\mu_{\Delta\psi_E}, \sigma_{\Delta\psi_E}^2), \end{aligned}$$

the time delay distance is given by:

$$\begin{aligned} \text{Time Delay Distance} &\sim \mathcal{N}\left(d + \mu_{\Delta d} \right. \\ &\quad \left. + d(\mu_{\Delta\theta_S} + \mu_{\Delta\psi_E}), \sigma_{\Delta d}^2 \right. \\ &\quad \left. + d^2(\sigma_{\Delta\theta_S}^2 + \sigma_{\Delta\psi_E}^2)\right) \end{aligned}$$

Therefore, the phase difference between the chief and deputy

spacecraft, which is represented as $\mathcal{N}(\mu_{\theta_P}, \sigma_{\theta_P}^2)$, is given by:

Phase Difference (in radians) \sim

$$= \mathcal{N}\left(\frac{2\pi(d + \mu_{\Delta d} + d(\mu_{\Delta\theta_S} + \mu_{\Delta\psi_E}))}{\lambda}, \frac{4\pi^2(\sigma_{\Delta d}^2 + d^2(\sigma_{\Delta\theta_S}^2 + \sigma_{\Delta\psi_E}^2))}{\lambda^2}\right)$$

$$\mu_{\theta_P} \text{ (in radians)} = \frac{2\pi(d + \mu_{\Delta d} + d(\mu_{\Delta\theta_S} + \mu_{\Delta\psi_E}))}{\lambda}$$

$$\sigma_{\theta_P}^2 \text{ (in radians)} = \frac{4\pi^2(\sigma_{\Delta d}^2 + d^2(\sigma_{\Delta\theta_S}^2 + \sigma_{\Delta\psi_E}^2))}{\lambda^2}$$

Uplink Array power, for statistically independent phases, is computed as [4]:

$$\text{Net Power} = P(N + N(N - 1)e^{-\sigma_{\theta_P}^2}),$$

where N is number of agents and P is the power transmitted by each agent. The power loss in dB is given by:

$$\text{Power Loss (dB)} = 10 \log_{10} \frac{(N + N(N - 1)e^{-\sigma_{\theta_P}^2})}{N^2}$$

The power loss for different wavelengths for different methods of metrology are shown above.

ACKNOWLEDGEMENTS

© 2018 California Institute of Technology. Government sponsorship acknowledged. This research was carried out at the Jet Propulsion Laboratory, California Institute of Technology, under a contract with the National Aeronautics and Space Administration. Many thanks to Dr. David Hansen (JPL, retired) for providing the link budget, to Dr. Stephen Townes (JPL) for providing technical guidance, to Dr. Fred Hadaegh for programmatic guidance, and to prof. Soon-Jo Chung of Caltech, and his student Yashwant Nakka, for technical discussions.

REFERENCES

- [1] Achieving Science with CubeSats: Thinking inside the box, National Academy of Sciences, 2016
- [2] R.E. Hodges, D.J. Hoppe, M.J. Radway, N.E. Chahat, "Novel Deployable Reflectarray Antennas for CubeSat Communications (Invited)", IEEE MTT Int. Symp., Phoenix, AZ, May 20, 2015.
- [3] E. Mettler, W. G. Breckenridge, and M. B. Quadrelli: Large Aperture Telescopes in Formation: Modeling, Metrology, and Control, The Journal of the Astronautical Sciences, vol. 53, no.5 October-December 2005, pp.391-412.
- [4] V. Vilnrotter, "Power spectrum of Uplink Array signals with random phase and delay errors", IEEE Aerospace Conference, Big Sky, MT, 2012.
- [5] G. M. Resch, T. A. Cwik, V. Jamnejad, R. T. Logan R. B. Miller, D. H. Rogstad: "Synthesis of a Large Communications Aperture Using Small Antennas", JPL Publication 94-15, July 1, 1994.
- [6] F. Tassi: "Lagrangian and Eulerian Multi-Scale Control of a Distributed Multibody Robotic System", M.S. Thesis, Politecnico of Milano, Italy, March 2018.

- [7] S. Bevilacqua: "Model derivation and dynamics propagation of multi-body tethered systems", M.S. Thesis, Politecnico of Milano, Italy, March 2018.
- [8] R. C. Clauss, R. B. Lovick, N. R. Mysoor, and J. Zitzelberger: "Antenna Cluster for Spacecraft High Effective Isotropic Radiated Power (EIRP) Applications", IPN Progress Report 42-158, August 15, 2004.
- [9] W. D. Williams, M. Collins, R. Hodges, R. S. Orr, O. S. Sands, L. Schuchman, H. Vyas: "High-Capacity Communications from Martian Distances". NASA/TM-2007-214415, December 2007.
- [10] N. Chahat, R. E. Hodges, J. Sauder, M. Thomson, E. Peral, Y. Rahmat-Samii: "CubeSat Deployable Ka-Band Mesh Reflector Antenna Development for Earth Science Missions", IEEE Transactions on Antennas and Propagation, Vol. 64, no. 6, June 2016.
- [11] R. E. Hodges, N. Chahat, D. J. Hoppe, J. D. Vacchione: "A Deployable High-Gain Antenna Bound for Mars", IEEE Antennas and Propagation Magazine, April 2017.
- [12] F. Y. Hadaegh, D. P. Scharf, S. R. Ploen, V. Jamnejad: "Reconfigurable Control for Formation of Antennas in Earth Orbit", IFAC Telematics Applications in Automation and Robotics, Espoo, Finland, 2004.
- [13] F. Y. Hadaegh, V. Jamnejad, D. P. Scharf, S. R. Ploen: "Self-organizing Control for Space-Based Sparse Antennas", Intech 2003; December 17, 2003; Chiang Mai; Thailand, 2003.
- [14] Small Spacecraft Technology State of the Art, NASA/TP-2015-216648/Rev1, Dec. 2015.
- [15] Chung et al.: Review of Formation Flying and Constellation Missions Using Nanosatellites, Journal of Spacecraft and Rockets, vol. 53, No. 3, May-June 2016.
- [16] Chung, S.-J., and Hadaegh, F. Y. Swarms of femtosats for synthetic aperture applications. In 4th international conference on spacecraft formation flying missions and technologies. St-Hubert, Quebec. May 18-20, 2011.
- [17] Castillo et al: Planetary Science enabled by the New Generation of Smallsats and miniaturized scientific instruments, IAA Sept.2017.
- [18] Quadrelli B.M., et al: Modeling and Dynamics Analysis of Tethered Formations for Space Interferometry, Advances in the Astronautical Sciences, vol. 108 pp. 1259-1278.
- [19] Quadrelli B.M., et al: Formations of Tethered Spacecraft as Stable Platforms for Far IR and Sub-mm Astronomy, presented at the Far IR and Submm Space Astronomy Workshop, University of Maryland College Park, March 6 2002.
- [20] Quadrelli B.M., et al: Dynamics and Control of Novel Orbiting Formations with Internal Dynamics, in The Journal of the Astronautical Sciences, vol.51, no. 3, July-September 2003, pp. 319-337.
- [21] Quadrelli B.M., et al: Formation Pointing Dynamics of Tether-Connected Architecture for Space Interferometry, in The Journal of the Astronautical Sciences, Vol. 52, No. 4, October-December 2004, pp. 475-493.
- [22] Quadrelli B.M., et al: Retargeting Dynamics of a Linear Tethered Interferometer, in the Journal of Guidance, Control, and Dynamics, vol. 27, no. 6, 2005, pp.1061-1067.
- [23] M. Quadrelli, D. Arumugam: Dynamics and Control of Microwave Granular Imager, presented at IEEE Aerospace Conference, Big Sky, MT, March 2018.
- [24] D. Morgan, S.-J. Chung, L. Blackmore, B. Acikmese, D. Bayard, and F. Y. Hadaegh, "Swarm-Keeping Strategies for Spacecraft under J2 and Atmospheric Drag Perturbations," JGCD, 2012.
- [25] C.A. Balanis: "Antenna Theory Analysis and Design" 2nd edition by Constantine A. Balanis. Published Wiley, 1984.
- [26] Morgan D., and Chung S.-J., Model Predictive Control of Swarms of Space- craft Using Sequential Convex Programming, Journal of Guidance, Control, and Dynamics, Vol. 37, No. 6, November-December 2014.
- [27] <https://www.jpl.nasa.gov/cubesat/missions/marco.php>
- [28] https://en.wikipedia.org/wiki/Jupiter_Icy_Moons_Orbiter

BIOGRAPHY



Marco Quadrelli is an internationally renowned expert in modeling for dynamics and control of complex space systems. He has a Masters Degree in Aeronautics and Astronautics from MIT and a PhD in Aerospace Engineering from Georgia Tech. He was a visiting scientist at the Harvard-Smithsonian Center for Astrophysics, and a lecturer at the Caltech Graduate Aeronautical Laboratories. After joining NASA JPL in 1997 he has contributed to a number of flight projects including the Cassini---Huygens Probe, Deep Space One, the Mars Aerobot Test Program, the Mars Exploration Rovers, the Space Interferometry Mission, the Autonomous Rendezvous Experiment, and the Mars Science Laboratory, among others. He has been the Attitude Control lead of the Jupiter Icy Moons Orbiter Project, and the Integrated Modeling Task Manager for the Laser Interferometer Space Antenna. He has led or participated in several independent research and development projects in the areas of computational micromechanics, dynamics and control of tethered space systems, formation flying, inflatable apertures, hypersonic entry, precision landing, flexible multibody dynamics, guidance, navigation and control of spacecraft swarms, terramechanics, and precision pointing for optical systems. He is an Associate Fellow of the American Institute of Aeronautics and Astronautics, a NASA Institute of Advanced Concepts Fellow, and a Caltech/Keck Institute for Space Studies Fellow.



Richard E. Hodges received the B.S. degree from the University of Texas at Austin, the M.S. degree from California State University, Northridge and the Ph.D. degree from the University of California Los Angeles, all in electrical engineering. From 1978 to 1984, he was with the Hughes Aircraft Company Radar Systems Group, Culver City, CA, where he performed design and analysis of electronic scanned array antennas, bandpass radomes, radiating elements (slots, printed circuit radiators, polyrods, etc.), and RF feed networks. In 1984, he joined the Adams-Russell Microwave Products Division, Chatsworth, CA (now Rantec Microwave Systems) where he developed waveguide-fed slot antennas for military radar applications. From 1988 to 1992, he was with NASA's Jet Propulsion Laboratory, Pasadena, CA, where he developed reflector antenna analysis software for the Deep Space Network, and coupled Finite-Element/Integral Equation code for the Parallel Computational Electromagnetics group. From 1992 to 1997, he was with UCLA performing research on electromagnetic modeling of complex radiators mounted on arbitrarily shaped bodies using the Hybrid Electric/Magnetic Field Integral Equation method and also worked as a Consultant to industry. From 1997 to 2001, he was with Raytheon's Antenna/Nonmetallics Technology Center, McKinney, TX, where he was the Technical Lead on Raytheon's DARPA RECAP program, which resulted in development of the world's first decade bandwidth (10:1) electronic scanned array antenna. At Raytheon, he also worked on a military airborne radar reflector antenna design and space-based electronic scanned array research. In 2001, he returned to the Jet Propulsion Laboratory where he is a Principal Engineer performing research and development on space-based antennas for radar and telecommunications. He was the Technical Group Supervisor of JPL's Spacecraft Antennas Group from 2002-2018 and Principal Investigator for numerous projects including the Integrated Solar Array and Reflectarray (ISARA) CubeSat project, the Mars Cube One (MarCO)

reflectarray antenna, the Instrument Incubator Program that led to the SWOT radar interferometer antenna, etc. His research interests include spaceborne deployable reflectarray antennas, deployable reflectors, waveguide slot array antennas and 3D printed lens antennas.



Victor Vlnrotter (M'79, SM'02) received his Ph.D. in electrical engineering and communications theory from the University of Southern California in 1978. He joined the Jet Propulsion Laboratory, Pasadena, Calif., in 1979, where he is a Principal Engineer in the Communications Architectures and Research section. His research interests include electronic compensation of large antennas with focal-plane arrays, adaptive combining algorithms for antenna arrays, optical communications through atmospheric turbulence, the application of quantum communications to deep-space optical links, and the development of uplink array calibration and tracking technologies. He has published extensively in conferences and refereed journals, and has received numerous NASA awards for technical innovations.



Saptarshi Bandyopadhyay is currently a Robotics Technologist at the Jet Propulsion Laboratory (JPL), California Institute of Technology (Caltech). He received his Ph.D. in Aerospace Engineering in January 2016 from the University of Illinois at Urbana-Champaign, supervised by Prof. Soon-Jo Chung from Caltech and Dr. Fred Hadaegh from JPL. He received his Dual Degree (B.Tech and M.Tech) in Aerospace Engineering in 2010 from the Indian Institute of Technology Bombay, India. His research interests include aerospace systems, robotics, multi-agent systems and swarms, dynamics and controls, estimation theory, probability theory, and systems engineering.